

Analysis of Four-dimensional Variational State Estimation of the Hawaiian Waters

Dax Matthews, University of Hawai‘i at Mānoa, Department of Oceanography, Marine Sciences Building, 1000 Pope Road, Honolulu, Hawai‘i 96822, USA. (matthews@hawaii.edu)

Brian Powell, University of Hawai‘i at Mānoa, Department of Oceanography, Marine Sciences Building, 1000 Pope Road, Honolulu, Hawai‘i 96822, USA. (powellb@hawaii.edu)

Ivica Janeković, University of Hawai‘i at Mānoa, Department of Oceanography, Marine Sciences Building, 1000 Pope Road, Honolulu, Hawai‘i 96822, USA. On leave from Institute Rudjer Bošković. (ivica@soest.hawaii.edu)

Abstract. In this study, we evaluate results from an incremental strong constraint four-dimensional variational data assimilation (IS4D-Var) experiment applied to the circulation around the Hawaiian Islands using the regional ocean model system (ROMS). Assimilated observations include: (a) satellite derived high-resolution swath radiometer sea surface temperatures (SST) and along-track altimetric sea surface heights (SSH) and (b) *in situ* temperature and salinity profiles from Argo floats, autonomous Seagliders, and shipboard CTD (conductivity, temperature, depth). Two assimilation configurations are compared: adjusting initial conditions versus adjusting both initial conditions along with atmospheric forcing. In the latter case, we compare two separate forcing products. For all experiments, we investigate how the assimilation alters the tidal, inertial, and mesoscale variability. Significant improvements in the observation-model fit are found for SST and salinity regardless of assimilation configuration or atmospheric forcing; however, significant change to the subsurface temperature is made when adjusting only initial conditions. Baroclinic tides are altered during the assimilation due to changes in the density field in regions of strong internal tide generation. Spurious inertial oscillations are found in assimilation circulations that are associated with the IS4D-Var increment when using either SST or SSH observations; however, this increase in the inertial energy had minimal effect on the mesoscale variability.

1. Introduction

1 Data assimilation is the process of combining observations and a numerical model to
2 produce an optimal estimate of the system. The goal of time-dependent variational as-
3 similation (4D-Var) is to use the dynamics of the model to determine an initial state,
4 boundary conditions, and atmospheric forcing that minimize a scalar function measuring
5 the distance to the observations [Talagrand and Courtier, 1987; Courtier et al., 1994].
6 The incremental approach, which is an approximation to 4D-Var, allows for a significant
7 improvement to the cost/benefit trade-off by working with linear increments to the state
8 [Courtier et al., 1994]. A complete 4D-Var system has been developed within the Regional
9 Ocean Modeling System (ROMS) model and is comprehensively described in Moore et al.
10 [2011c]. In this study, we employ the incremental strong constraint 4D-Var (IS4D-Var) to
11 adjust the initial conditions and atmospheric forcing, assuming that the model physics do
12 not contain errors. The mentioned ROMS IS4D-Var system has been previously used to
13 study ocean dynamics in several regions [Powell et al., 2008; Broquet et al., 2009; Zhang
14 et al., 2010; Moore et al., 2011a, b].

15 Our model domain covers the Hawaiian Islands (Figure 1) located in the southern
16 portion of the North Pacific Gyre, characterized with the presence of nearly persistent
17 northeastward trade winds that have a significant effect on both ocean currents and winds
18 [Xie et al., 2001]. The mountain peaks on the islands of Maui and Hawai‘i penetrate the
19 trade wind inversion layer, deflecting the wind flow around the islands – creating a large
20 wake region of weakened flow [Smith and Grubii, 1993]. An active and intense eddy field
21 lies in the wake region (Figure 1b), driven primarily by the wind stress curl and intrinsic

22 instabilities in the ocean flow [Calil et al., 2008; Yoshida et al., 2010]. Variability is
23 also increased due to both baroclinic and barotropic instabilities in the mean flow [Chen
24 and Qiu, 2010] in the northwest of the domain. Furthermore, the Hawaiian Islands are a
25 significant site for the generation of internal waves due to tidal flow over steep topography
26 [Merrifield et al., 2001; Ray and Mitchum, 1996]. Vertical tidal motions of the thermocline
27 are commonly observed in the region with amplitudes of over 10 m [Chiswell, 1994] and
28 can peak above 90 m along tidal beams that originate on both sides of the ridge [Carter
29 et al., 2008].

30 The North Equatorial Current (NEC) flows from east to west, intensifying in the south-
31 ward direction east of the island chain (Figure 1a). The mean ocean circulation in lee of
32 the islands forms a canonical pattern [Lumpkin, 1998; Flament et al., 1998] with four ma-
33 jor current systems. The NEC impinges on the Island of Hawai‘i and bifurcates, with most
34 of the current flowing southwest past the island chain. The North Hawaiian Ridge Current
35 (NHRC) flows northwest along the windward side of the islands. Along the leeward side
36 of the island chain, from Maui to Kaua‘i, the Hawaiian Lee Current (HLC) flows north-
37 west, parallel to the NHRC. The Hawaiian Lee Counter Current (HLCC), which forms in
38 response to the wind stress wake of the islands, flows counter to the NEC [Xie et al., 2001]
39 along 19°N. Surface water temperatures in the region have a strong meridional gradient
40 and a slight zonal gradient (Figure 1a), with warmer water in the southwest due to the
41 HLCC [Lumpkin, 1998] having an annual cycle variation between an average of 23°C in
42 winter and 27°C in summer.

43 The main objective of this study is to examine the skill and performance of the data
44 assimilation system for the Hawaiian ocean state modeled at a submesoscale resolution

45 by producing analyses of the dynamics over a two year time period (2008-2010). The
46 assimilation system experiment uses two different configurations: in 2008 only the ini-
47 tial conditions of the model are adjusted, while in 2009, both the initial conditions and
48 the atmospheric forcing are adjusted. Broquet et al. [2011] showed that without surface
49 forcing adjustment the assimilation could degrade the temperature structure at depth;
50 however, adjusting the surface forcing can lead to abnormal temporal and spatial vari-
51 ability in the forcing fields. In our study, we assimilate a significant number of remote and
52 *in situ* observations of the circulation, including: high-resolution, minimally processed,
53 non-blended (temporally or spatially) satellite observations using validated sea surface
54 temperature (SST) swath data and along-track sea surface height (SSH) data, along with
55 *in situ* temperature and salinity data from autonomous Seagliders, Argo floats, and ship-
56 board conductivity, temperature, salinity (CTD) profiles.

57 We evaluate the performance of an IS4D-Var system in a complex island domain with
58 strong barotropic and baroclinic tides, large mesoscale eddies, complex submesoscale in-
59 teractions, and dominant atmospheric forcing by comparing how well the model can re-
60 produce the observations with the consistency of the errors. Furthermore, we compare
61 the dynamical adjustments made to the model when perturbing either or both the initial
62 conditions and atmospheric forcing. Finally, we discuss the resulting circulation and how
63 adjustments affect the estimates of the tides, inertial, and mesoscale flows. Each of these
64 objectives is presented in sections below, followed by concluding remarks at the end.

2. Data assimilation system

2.1. IS4D-Var theory

For our study, we utilize the IS4D-Var system within ROMS model based on the formulation of Courtier et al. [1994], using the Adjoint and Tangent Linear models [Moore et al., 2004, 2011c]. In this section, we briefly present the principles of IS4D-Var, encouraging the reader to the more detailed description in Moore et al. [2011c]. 4D-Var has several advantages over other methods used to combine observations with an ocean model, such as optimal interpolation (OI) or 3D-Var. Our goal is not to compare the relative merits of each, but a review can be found in Lorenc [2006]. The two main advantages of 4D-Var are that the time-variable dynamics of the model are used to evolve the error covariances and many more constraints (via the observations) are available during a time window as opposed to a single time. These characteristics of 4D-Var are essential for this study because of the strong internal tides in the region that can heave the thermocline by as much as 90 m during a single M_2 cycle [Carter et al., 2008] and the use of Seaglider and Argo data where the internal tides cannot be removed due to their sampling characteristics.

The system is applied to time cycles of interval $[t_o, t_f]$, during which the model control variables (initial conditions, $\mathbf{x}(0)$, surface forcing, $\mathbf{f}(t)$, and boundary conditions, $x_{bc}(t)$) are corrected to ensure that the model better agrees with the observations in a least-squares sense. The incremental form determines the linear increments, $\delta\mathbf{z} = (\delta\mathbf{x}(0), \delta\mathbf{f}(t), \delta\mathbf{x}_{bc}(t))$ that should be applied to the control vector. These linear increments are integrated forward in time with the tangent-linear model, while the sensitivity of the quadratic cost-function to the increments is determined by the adjoint model.

The quadratic cost function that describes the difference to be minimized is defined as the combined penalty for deviating from the observations (\mathcal{J}_o) and initial guess (\mathcal{J}_b), as

given by:

$$\mathcal{J}_o = \frac{1}{2}(\mathbf{G}\delta z - \mathbf{d})^T \mathbf{R}^{-1} (\mathbf{G}\delta z - \mathbf{d}) \quad (1)$$

$$\mathcal{J}_b = \frac{1}{2}\delta \mathbf{x}(0)\mathbf{P}_b^{-1}\delta \mathbf{x}(0) + \frac{1}{2}\delta \mathbf{f}(t)\mathbf{P}_f^{-1}\delta \mathbf{f}(t) + \frac{1}{2}\delta \mathbf{x}_{bc}(t)\mathbf{P}_{bc}^{-1}\delta \mathbf{x}_{bc}(t) . \quad (2)$$

Where \mathbf{P}_b , \mathbf{P}_f , \mathbf{P}_{bc} , and \mathbf{R} are the assumed background, forcing, boundary condition, and observation error covariance matrices, \mathbf{G} is the tangent linear model sampled at the observation locations, \mathbf{G}^T is the adjoint of \mathbf{G} , and \mathbf{d} (or innovation vector) is the difference between the first guess and the observations. The optimal increment $\delta \mathbf{z}^a$ that minimizes \mathcal{J} is calculated using an iterative Lanczos formulation of the Conjugate Gradient (CG) algorithm [Fisher, 1998].

2.2. Model configuration

We model the Hawaiian Island region at a 4-km resolution with 30 s-levels, with ROMS, a free-surface, hydrostatic, primitive equation model discretized with a terrain following vertical coordinate system [Shchepetkin and McWilliams, 2005]. The domain spans 164°W to 153°W in longitude and 17°N to 24°N in latitude. The model bathymetry is based upon data from the Hawaiian Mapping Research Group, though slightly adjusted to minimize the effects of horizontal pressure gradient errors (HPGE). The mean HPGEs were found to be less than 7 cm/s around the island chain. The baroclinic time step is 450 seconds and due deep waters in the domain the baroclinic time step is less than 12 seconds. The boundary conditions are configured to conserve volume using a Chapman condition of the free surface [Chapman, 1985], a Flather condition for the 2D momentum, and clamped for the 3D momentum and tracers [Marchesiello, 2001]. A fourth-order Akima horizontal

¹⁰² advection scheme is used [Akima, 1984], along with the KPP vertical mixing scheme
¹⁰³ described in Large et al. [1994].

¹⁰⁴ The lateral boundary conditions are taken from Navy Coastal Ocean Model (NCOM)
¹⁰⁵ fields supplied by the Naval Research Laboratory (NRL) [Barron et al., 2006]. Due to im-
¹⁰⁶ balances between NCOM and ROMS we employ a sponge layer along the four boundaries
¹⁰⁷ with a width equal to one Rossby radius of deformation of the region (80 km). The model
¹⁰⁸ was additionally forced with eight primary (M_2 , S_2 , N_2 , K_2 , K_1 , O_1 , P_1 , Q_1), two long
¹⁰⁹ period (M_f , M_m), and one non-linear (M_4) barotropic tidal constituents from the Oregon
¹¹⁰ State University TOPEX/Poseidon tidal product, TPXO7.1 [Egbert et al., 1994] in all
¹¹¹ experiments. There are two distinct periods using differing atmospheric forcing prod-
¹¹² ucts in our study: the first, is a combination of the NCEP-CORA wind product [Milliff
¹¹³ et al., 2004] that combines NCEP winds (2°) with observed Quikscat winds (0.5°) that we
¹¹⁴ have combined with winds from a fine-scale (9km) PSU/NCAR mesoscale model (MM5)
¹¹⁵ [Yang et al., 2008a]. The MM5 winds are statistically blended with the NCEP-CORA
¹¹⁶ winds to cover a domain larger than the available MM5 data. The other NCEP fields for
¹¹⁷ temperature, humidity, pressure, rain, and heat flux are used at the coarse 2° resolution.
¹¹⁸ The second, from July of 2009, is a locally run, high-resolution Weather Regional Forecast
¹¹⁹ (WRF) model [Chen, personal comm.] that covers the entirety of the domain. The ROMS
¹²⁰ ocean surface heat flux is computed via the COARE algorithm of Fairall et al. [1996] using
¹²¹ information from the atmospheric models. We apply a monthly mean heat flux correction
¹²² to balance the climatological NCOM SST with either MM5 or WRF, depending on the
¹²³ period of simulation, to account for any heat flux imbalance between the state of the ocean
¹²⁴ and the atmospheric forcing. This correction is made to balance the incoming boundary

₁₂₅ conditions which are in balance with a different atmosphere than those forced with the
₁₂₆ global NCEP fluxes.

2.3. Observations

₁₂₇ Observational data are taken from all available products at their native resolutions, with
₁₂₈ satellite SST and SSH providing observations of the ocean surface, while shipboard CTD,
₁₂₉ ARGO floats, and autonomous Seagliders provide observations of the ocean interior.

₁₃₀ SST observations are taken from the Global Ocean Data Assimilation Experiment High
₁₃₁ Resolution Sea Surface Temperature (GHRSST) Level 2 Preprocessed (L2P) sea sur-
₁₃₂ face temperature data set distributed by the Physical Oceanography Distributed Active
₁₃₃ Archive Center (PO.DAAC) from both the Advanced Very-High Resolution Radiometer
₁₃₄ (AVHRR) and the Moderate Resolution Infrared Spectroradiometer (MODIS) sensors.

₁₃₅ These observations have a 1.1 km spatial resolution and give estimates of SST that are
₁₃₆ nominally accurate to 0.5°C [McClain et al., 1985]. The MODIS sensor is onboard the
₁₃₇ polar orbiting NASA AQUA and TERRA satellites with timed orbits such that TERRA
₁₃₈ passes from north to south across the equator in the morning and AQUA passes in the
₁₃₉ afternoon. This setup provides two primary satellite passes per day at approximately 2
₁₄₀ AM and 2 PM local time; however, due to the large swath, multiple passes of the satellite
₁₄₁ capture portions of our domain. A higher number of SST observations are available in
₁₄₂ lee of the islands due to the westerly reversal blocking of the winds that keep the island
₁₄₃ wakes cool and nearly free of clouds during the day [Yang et al., 2008a].

₁₄₄ We also use the along-track sea level anomaly (SLA) product produced by Ssalto/Duacs
₁₄₅ and distributed by Archiving Validation and Interpretation of Satellite Oceanographic
₁₄₆ data (AVISO), with support from Centre National d'Etudes Spaciales (CNES), from the

¹⁴⁷ altimeters onboard the Jason-1, Jason-2, Envisat, and Geosat Follow On (GFO) satellites.
¹⁴⁸ The along-track resolution is \sim 6 km for Jason-1 and Jason-2, \sim 7 km for Envisat, and \sim 10
¹⁴⁹ km for GFO (Figure 1b). The cross-track resolution varies depending on the satellites
¹⁵⁰ overhead and their current orbital path. A mean sea surface from a 6-year run of the non-
¹⁵¹ linear model was added to the SLA data to generate SSH data that are consistent with the
¹⁵² model free-surface. We do not want to adjust the TPXO tidal forcing during assimilation,
¹⁵³ hence predicted tides from the non-linear model are added to the SLA observations such
¹⁵⁴ that tidal-frequency signals should not be considered in the assimilation cycle. One caveat
¹⁵⁵ in the assimilation of SSH data is that the adjoint model may identify a sensitivity to
¹⁵⁶ gravity waves that are capable of resolving the model and observation difference (see
¹⁵⁷ Powell et al. [2009]). Although dynamically correct, spurious gravity waves are not an
¹⁵⁸ appropriate signal to be added during the assimilation. To prevent this, we replicate each
¹⁵⁹ altimeter observation at $t = [t_o - 6, t_o - 4, t_o - 2, t_o, t_o + 2, t_o + 4, t_o + 6]$ hours, but with the
¹⁶⁰ appropriate tidal elevation. Here we assume high temporal correlation of the sub-tidal
¹⁶¹ altimeter data, as the sampled altimeter mesoscale field does not change significantly over
¹⁶² 12 hours.

¹⁶³ For this experiment, *in situ* depth profiles of temperature and salinity are provided by
¹⁶⁴ three different platforms: Argo floats, autonomous Seagliders, and shipboard CTD. The
¹⁶⁵ Argo program is a global array of vertical profiling floats that provide temperature and
¹⁶⁶ salinity profiles every 10 days at depths ranging from the surface to 2000 m [Oka and Ando,
¹⁶⁷ 2004]. We only use data during the ascension and descension of the Argo float (locations
¹⁶⁸ of Argo surfacings are shown in Figure 1d), during which samples are taken every 10 m
¹⁶⁹ vertically. The University of Hawai‘i operates a number of autonomous, buoyancy driven

170 Seagliders in the region that are capable of predefined mission dives and can sample
171 temperature and salinity from the surface to 1000 m. The Seaglider missions used were
172 part of the Hawai‘i Ocean Time-series (HOT) program [Karl and Lukas, 1996] and Hawai‘i
173 Ocean Observing System (HiOOS) primarily around the island of O‘ahu (Figure 1c). Due
174 to the nature of the Seaglider motion, horizontal and vertical resolutions are variable. Also
175 from the HOT program, we utilize temperature and salinity profile data from monthly
176 HOT cruises taken to the deep-water Station ALOHA (A Long-Term Oligotrophic Habitat
177 Assessment) site located 100 km north of the island of O‘ahu.

178 Because a majority of the considered observations are at a higher spatial resolution
179 than the model, observations are spatially averaged into bins that relate to the grid cells
180 of the model, while preserving the time of observation. This procedure removes small-
181 scale features in the observations, not represented by the model, and allows for an error
182 of representativeness to be estimated from the observational variance present in each bin.
183 All observations within a Rossby radius distance from the model open boundaries are
184 removed from consideration because of the strong sponge layer in the region to mitigate
185 inconsistencies with the boundary conditions.

186 In IS4D-Var the difference between each observation and model is weighted by the
187 observation error of representativeness covariance matrix (\mathbf{R}); although, it is formally
188 a covariance matrix, we use a diagonal variance matrix of size equal to the number of
189 observations. The variance assigned to each observation is the maximum of either: the
190 variance calculated from the gridding procedure above, the instrument error or the geo-
191 physical time-variability of each observational product. The noise level was found using a
192 semivariogram technique [Matthews et al., 2011] or from a residual spectra method [Zanifé

et al., 2003]. An estimate of the geophysical time variance was found from multiple year time-series of each observation product. In the case of SST, we generated monthly maps of variance using 5-years of daily global level-3 MODIS and pathfinder AVHRR data provided by PO.DAAC. Monthly maps of SSH variance were generated using all data from each satellite starting after January 2000. For *in situ* observations, variance was calculated as a function of depth using 20 m bins from the surface to the maximum depth. Temperature and salinity data from 20 years of HOT profiles, 8 years of Argo profiles, and 2 years of various Seaglider missions were used to estimate the geophysical variance for each of the observation platforms.

We only used MODIS data to provide SST because of the large number of SST observations; however, from March 2009 to June 2009 the MODIS data was cloud contained, as many observations were too cold for the tropics (less than 18°C). We assimilated only SST data from AVHRR NOAA-18 during this period. The cloud filter problem was resolved by July 2009 and MODIS data were used for the remainder of the study. Finally, the primary AVISO high-resolution, along-track data is provided in delayed time. At the time of these experiments, the data were only available through July 2009, after which the AVISO near-realtime, variable alongtrack (~ 20 km) resolution product was used, resulting in far fewer SSH observations.

After the gridding procedure, nearly 27 million observations were created for the two year period, of which 94.5% were SST from satellite radiometers, 3.7% from SSH altimetry, and 1.65%, 0.1%, and 0.4% were temperature and salinity observations from Seagliders, Argo floats, and HOT cruise CTD, respectively. Our goal is to use as many available

²¹⁵ data (particularly, *in situ*), but by withholding AVHRR data we are able to examine the
²¹⁶ assimilation system against an independent set of observations.

2.4. Data assimilation setup

²¹⁷ There are several parameters required to be determined *a priori* to the assimilation. The
²¹⁸ length of the assimilation time cycle should not exceed the period for which the tangent
²¹⁹ linear assumption is valid for incremental 4D-Var methods. A particularly energetic period
²²⁰ was chosen (7/12/2008-7/19/2008) to perform an ensemble experiment to determine this
²²¹ time length. Orthonormal perturbations were generated (as per Powell et al. [2008]) and
²²² integrated separately by the nonlinear and tangent-linear models. Ensemble root-mean-
²²³ square (RMS) and correlations between the perturbed nonlinear (NLM) and tangent-
²²⁴ linear (TLM) solutions were then compared to determine consistency. The assumption
²²⁵ of linearity is no longer valid once the solutions deviate, providing an estimate of the
²²⁶ maximum time that should be used for the assimilation window. The results showed that
²²⁷ after 4.5 to 5 days the NLM and the TLM are no longer consistent. A 4-day assimilation
²²⁸ cycle length was chosen for all experiments from this information.

²²⁹ Twenty inner-loops were used for the experiments, as further loops provided little re-
²³⁰ duction in the cost-function. For some periods, due to strong tidal currents along steep
²³¹ slopes, the model time-step was reduced to maintain the CFL condition. The number of
²³² inner loops was slightly reduced such that the total integration time was similar during
²³³ these periods.

²³⁴ The background and forcing error covariance matrices (Eq. 2) constrain the analysis by
²³⁵ penalizing departures from the background state. Estimating \mathbf{P}_b , and \mathbf{P}_f is accomplished
²³⁶ through factorization [Weaver and Courtier, 2001]. Because the covariance terms are not

known directly, they are approximated by a Gaussian diffusion of the standard deviations over specified length-scales. The standard deviations were computed from monthly climatologies based upon a 6-year run of the NLM, such that each cycle used its monthly variance. Background length scales for the diffusion were calculated using the semivariogram technique on multi-year time series of satellite and *in situ* data sets described in detail in Matthews et al. [2011]. Horizontal length scales of 150 km were chosen for free surface and velocity with 170 km for temperature and salt. Vertical length scales were set to 50 m for velocity, 140 m for temperature, and 240 m for salt. Surface forcing length scales were set to 50 km for wind stress and 250 km for heat and salt flux.

2.5. Experiment setup

This IS4D-Var experiment of circulation around the Hawaiian Islands is performed for the period of January 1, 2008 through December 31, 2009. We compare the IS4D-Var system to a control run without data assimilation (deemed FWD) through statistical measures of model performance. The assimilation experiment is performed in two stages. In 2008, only initial conditions are adjusted during the assimilation cycles (deemed NF08), while in 2009, initial conditions are adjusted and surface forcing is corrected every 12 hours (deemed F09). Because of the switch in atmospheric forcing in July, 2009, we decompose the F09 experiment into F09M, which refers to the analysis circulations with forcing adjustment and MM5/NCEP forcing, and F09W, which refers to the analysis circulations with forcing adjustment and WRF forcing. The experiments are summarized in Table 1.

3. Results

3.1. Comparison between the model experiments and observations

In this section, we explore the effects of the different assimilation configurations, atmospheric forcings, and observational products on the model performance. Over the two-year study period the observational contribution to the cost function is 86.1%, 3.4%, 3.9%, and 6.2% for SST, temperature at depth, salinity, and SSH, respectively. The assimilation system reduces the root mean squared error (RMSE) between observations and the model by 0.21 K, 0.21 K, 0.072, and 0.013 m, which corresponds to a reduction of 37%, 22%, 40%, and 12%, in SST, temperature at depth, salinity, and SSH, respectively, as compared against the FWD case. While the correlation coefficient (CC) between the observations and the model are high in the FWD experiment (above 0.89), the assimilation still makes improvements of 3%, 0.5%, 3.1%, and 1.4% for SST, temperature at depth, salinity and SSH, respectively.

Comparing the assimilation system against the AVHRR SST data withheld during the assimilation, we find that it reduces the total RMSE by 0.1 K compared to the FWD experiment and increases the correlation from 0.94 to 0.95. However, significantly larger corrections are found directly in lee and south of the Island of Hawai‘i and in the Alenuihaha Channel (between Maui and Hawai‘i), where RMSE is reduced from the FWD experiment by over 0.4 K.

Figure 2 shows the RMSE between the model and observations, with the average observational error assigned for each 4-day assimilation cycle. Similarly, Figure 3 shows the CC between the model and observations for each 4-day cycle. The average observational error assigned to the delayed time SSH data is 5.5 cm and 6.5 cm for the near real-time product. The SSH RMSE shows no trend until the switch to real-time data on 7/17/2009, at which the RMSE between the observations and the FWD experiment increases by 2

cm due to a reduction of quality control in the real-time data (Figure 2a). Because the change in SSH observational products nearly coincides with the change in the atmospheric forcing, we conducted a short, additional 36 day test to determine whether the change in forcing may also be contributing to the increased RMSE. Our findings show that during the test period, the SSH RMSE was unaffected by the change in atmospheric forcing. Also, no significant difference in SSH RMSE is found when comparing NF08 and F09M. The reduction of RMSE between the FWD and analyses is limited to an average of 11.6 cm (improvement of 4.6%) when using the near real-time data, compared to 9.4 cm from the delayed-time product (improvement of 12.5%). The average reduction of RMSE from Jason-1 and Jason-2 (15.4% and 14.9%) is larger than that from Envisat and GFO (9.6% and 7.4%). This is likely due to an increase in noise levels in the Envisat and GFO data relative to Jason-1 and Jason-2, which from residual spectral methods was found to be 2 cm larger. The SSH CC for the experiments are: FWD 0.88, NF08 0.89, F09M 0.91, and F09W 0.85.

The RMSE between the SST and FWD increases in 2009 due to the change from MM5/NCEP to WRF for atmospheric forcing on 7/26/2009 (Figure 2b). The average SST RMSE from FWD is 0.41 K, 0.52 K, and 0.79 K during the NF08, F09M, and F09W periods. All assimilation experiments reduced the SST RMSE to average values of 0.34 K, 0.35 K, and 0.39 K for NF08, F09M, and F09W respectively, which is close to the average SST observational error of 0.31 K. Figures 4a and 4b shows a map of SST RMSE from FWD and a combination of the NF08, F09M, and F09W experiments, respectively. The highest errors in FWD, with values greater than 0.8 K, are found in the lee of the island of Hawai‘i and in the Alenuihaha Channel. Decorrelation length scales are reduced and

variability is increased [Matthews et al., 2011] in lee of the island of Hawai'i, also there is a strong diurnal variation in SST due to increased variability in heat flux from a reduction in cloud cover [Yang et al., 2008b]. The assimilation reduces the RMSE for SST to less than 0.4 K away from the Hawaiian lee and to less than 0.6 K in the lee in all assimilation experiments. Overall, the state estimation is performing exceptionally well with respect to the SST; however, the strong diurnal variability in the lee is not adequately captured by the models. We address the comparison between model and observed SST in detail in Section 3.3.

RMSE between the experiments and *in situ* temperature observations are shown in Figure 2c. For subsurface temperature, the average RMSE is 0.78 K, 0.74 K, and 0.63 K for NF08, NF09M, and NF09W, respectively. This is a reduction of 6%, 26%, and 42% as compared to FWD. The *in situ* observational error is primarily chosen to be the instrument error. These observations are taken in regions of strong baroclinic tides that heave the isopycnals by as much as 100 m [Carter et al., 2008]. A numerical model with coarser resolution and bathymetry than reality will not capture the precise phase of the baroclinic tide; hence, an internal wave with a 5 minute phase shift can result in significant differences between the *in situ* and modeled values. On reflection, using the instrument error to capture the representation of *in situ* observations was a mistake, but rather an error should have been used that is indicative of possible phase changes in propagating internal tides. Large reductions of *in situ* salinity RMSE, compared to FWD, are found (Figure 2d) in each assimilation experiment, with values of 45%, 55%, and 47% in NF08, F09M, and F09W, respectively. We relaxed the surface salinity flux towards climatology in the NF08 experiment , which introduced a 0.2 reduced salinity bias when

compared to observations in the mixed layer of the FWD experiment. This bias then was reduced to 0.15 in the NF08 experiment. Significant variability exists in the reduction of RMSE, when compared to FWD, between the different *in situ* platforms. The Seaglider observations dominate the number of *in situ* observations when they are available and provide the greatest reduction in RMSE.

3.2. Consistency of background error covariance

We examine the consistency of our specified error covariance matrices using a set of diagnostics described in Desroziers et al. [2009]; Moore et al. [2011a]. These diagnostics are based on the innovation vector and consider the projection of the background and analysis into observation space. Desroziers et al. [2009] determine the posterior observation and background error variances using:

$$(\tilde{\sigma}_i^b)^2 = \frac{1}{2} \sum_{j=1}^{p_i} (\mathbf{y}_j^a - \mathbf{y}_j^b)(\mathbf{y}_j^o - \mathbf{y}_j^b) \quad (3)$$

$$(\tilde{\sigma}_i^o)^2 = \frac{1}{2} \sum_{j=1}^{p_i} (\mathbf{y}_j^o - \mathbf{y}_j^a)(\mathbf{y}_j^o - \mathbf{y}_j^b) \quad (4)$$

where i refers to the observation type; p_i is the number of observations of that type; and y_j^a , y_j^b , and y_j^o refer to the analysis, background, and observation values, respectively. If the *prior* background and observation error covariance matrices are well specified, they will be consistent with the posterior values $(\tilde{\sigma}_i^b)^2$ and $(\tilde{\sigma}_i^o)^2$. Figure 5 shows the time-series of the *posterior* errors from the two-year assimilation experiments against the *prior* errors for the same observation points for salinity, SSH, SST (from satellite observations), and subsurface temperature (from *in situ* observations). For SSH, we found that the observation *prior* and *posterior* errors ($\bar{\sigma}_i^o > \tilde{\sigma}_i^o$) are consistent within a factor of 2, such that the *prior* is underestimating the actual error. As described earlier, the covariances

were artificially increased when adding the TPXO tides, and it seems that too much error was attributed. Worse, the background *prior* covariance did not remove the tidal signal, and so the background covariance error is significantly overestimated for SSH. For SST, the observation *prior* and *posterior* errors are consistent (Figures 5c and 5d), while the prescribed diurnal variance in the background is an overestimate of what is found in the *posterior*. For the *in situ* measurements, the variances used were all consistent and the overall results are consistent with those reported in both meteorological and oceanographic applications using data assimilation [Moore et al., 2011a]. The diagnostics suggest that improvements in the analysis would be seen if the SSH observation errors were increased and the background errors were decreased. This would affect the cost function by giving less weight to the innovation vector and reduce the penalties on differences between the analysis and background. However, one must keep in mind that the diagnosed observation and background errors shown in Figure 5 are not the true or optimal values, depending on the *a priori* choices of the errors, but can be used to characterize the *priori* estimates.

3.3. Temperature and heat flux adjustments

In this section, we focus on the analysis of the assimilating high-resolution satellite radiometry derived SST (that account for over 94% of all observations considered), in order to understand the differences in performances of the NF08 and the F09(M/W) experiments. 4D-Var theory assumes that the errors are unbiased; however, comparison between the FWD case and observations show biased SST regions. The upper model layer used to represent SST is 4 m thick on average because our domain is deep (> 5000 m) and ROMS uses a terrain following coordinate system. Satellite radiometers observe only the temperature of the skin layer of the ocean, rather than the bulk layer temperature

that is representative of the upper few meters of the ocean. The thickness of the skin layer is less than a millimeter [Grassl, 1976] and contains a sharp temperature gradient when wind speeds are less than 10 m/s [Clauss et al., 1970], above which wind induced waves destroy the skin layer. Differences between the skin and bulk temperatures (ΔT) measured more than a meter below the surface differ as much as 1 K [Robinson et al., 1984] and can vary as much in a single diurnal cycle [Schluessel et al., 1990]. Following Liu and Businger [1975], we estimate

$$\Delta T \cong Q_N \left(\frac{t_*}{\rho_w c_p \kappa} \right)^{\frac{1}{2}}, \quad (5)$$

where Q_N is the net surface heat flux, t_* is the surface renewal time scale, ρ_w is the density of seawater, c_p is the specific heat of the ocean at constant pressure and salinity, and κ is the molecular thermal conductivity. We calculated the bulk-skin temperature difference for data near 2 AM and 2 PM local time (the nominal time of MODIS passes) using the surface heat flux and wind stress from FWD. The temperature gradient between the bulk and skin layer is negligible except in the immediate lee of the islands where winds are reduced. The average daytime skin temperature is more than 0.2 K warmer than the bulk temperature in lee of the islands of Maui and Hawai‘i, while at night, the skin is 0.1 K cooler than the bulk temperature.

The bulk-skin temperature differences and 4 m representation of SST in the model lead to a bias between the observations and FWD. On average the FWD model is 0.3 K warmer than coincident SST observations, with large SST biases found in lee of the islands. The largest bias is found in the lee of the island of Hawai‘i where it is on average 0.7 K (warmer than observations). In numerical experiments with model forcing from WRF, the incoming solar shortwave radiation flux is larger than that from MM5/NCEP

368 forced models, showing an average increase of 200 W/m² in peak daytime hours. The
369 greater daytime heat flux increases the SST bias in FWD case to 1 K for several hundred
370 kilometers leeward of the island of Hawai‘i and in the Alenuihaha Channel.

371 The assimilation effectively removes the SST biases in both the NF08, F09M, and
372 F09W experiments to 0.03 K, 0.09 K, and 0.08 K, respectively, using different physical
373 mechanisms. The NF08 experiment only adjusts initial conditions and has no other way
374 to account for diurnal SST variability. Even so, the average SST bias from NF08 is smaller
375 than that from F09M and F09W; however, this is due to the inducing of a cold bias in
376 the NF08 system during peak daytime hours. Analysis of temperature observation/model
377 RMSE from subsurface *in situ* data gives further insight into how SST observations are
378 affecting the NF08 experiment. In the regions below 200 m, the reduction in RMSE and
379 bias are similar between NF08 and F09M, with RMSE below 0.7 K and a cold bias less
380 than 0.1 K. However, above 200 m depth both RMSE and bias from NF08 are higher than
381 values from coincident cycles of FWD. The largest increase is over 1 K at 50 m depth in
382 both RMSE and bias. The bias is unaffected in the F09M case and RMSE is below 0.7
383 K. Without surface forcing, the NF08 experiment generates upwelling in order to bring
384 colder waters to the surface to compensate for the diurnal fluctuation of SST, leading to
385 unrealistic and significantly colder temperatures in the upper 200 m layer.

386 On the other hand, by adjusting the surface heat flux the F09M and F09W experiments
387 have a time-dependent mechanism to account for some of the diurnal SST bias found
388 between the model and observations. Here the cold, daytime bias is removed, as is the
389 nighttime warm bias in the majority of the domain (except in the island channels and in
390 lee of the island of Hawai‘i where a warm bias of 0.2 K persists). Figure 6 shows time-

averaged maps of the adjustments made to the heat flux at 2 PM and 2 AM local time.

The daytime heat flux is increased over the majority of the domain by 25 W/m², while at night the heat flux is reduced at some places by more than 100 W/m², primarily in lee and south of the island of Hawai'i. The widespread distribution of the nighttime bias is likely due the average 4 m thick layer used to represent SST diurnal variability in the model.

In future assimilation experiments the model surface layer will ideally be significantly shallower. Also, models of upper ocean diurnal warming, such as the Profiles of Upper Ocean Heating (POSH) model developed by Gentemann et al. [2009], could be used to correct radiometric SST data for bulk/skin temperature differences prior to assimilation.

3.4. Salt flux and wind stress adjustments

During both the F09M and F09W experiments salt flux and wind stress are also adjusted during the minimization procedure. When using WRF forcing, the FWD model evaporates 60% less as compared to when using MM5/NCEP. However, while the surface salt flux is adjusted only 3% in the F09M experiment (with larger reductions of 10-15%) in the lee of Hawai'i), during F09W the salt flux is reduced by 30% over the entire domain. This result is counter-intuitive and is likely a response to the increased heat flux from WRF.

Time-averaged mean wind stress computed from MM5/NCEP and WRF models have similar values in both direction and magnitude, though the variability is higher in WRF case. Surface wind stress is relatively unchanged during the assimilation in both experiments. In F09M, westward zonal wind stress due to the trade winds is unaffected over a majority of the domain and reduced by only 2-3% in the Alenuihaha Channel and

413 south of Hawai‘i. Meridional wind stress is increased north of the island chain by 5–10%
414 and relatively unaffected elsewhere. Similar changes are found in the F09W experiment;
415 however, without the northward increase in wind stress.

3.5. Comparing coincident assimilations with and without forcing adjustment

416 In the results presented in Section 3.3, we show that without surface forcing adjustment,
417 the assimilation degrades the temperature structure at depth. Because there is
418 no temporal overlap between the NF08 and F09M/F09W experiments, we performed an
419 additional experiment to compare both assimilation configurations over the same time
420 period. We assimilated only satellite data and withhold the *in situ* observations as an
421 independent validation over 6 assimilation cycles from July 17, 2009 to August 6, 2009.

422 During this time a relatively large SST RMSE between the model and observations ex-
423 ists, which should maximize the subsurface effects when not allowing adjustments to the
424 surface forcing. Also during this time both atmospheric products were available, so the
425 initial 3 cycles used MM5/NCEP forcing and the final 3 use WRF. In this section we refer
426 to these two experiments as, EXNF, which refers to the assimilation analyses with only
427 initial condition correction, and EXF, which refers to analyses with both initial condition
428 and surface forcing correction.

429 The reduction in SST RMSE in the EXNF and EXF experiments is nearly identical
430 for each of the MM5/NCEP and WRF periods. However, the mean bias between SST
431 observations and the forecast circulations is increased by 0.2 K because of the increased
432 heat flux from the WRF model during those cycles.

433 We compare against observations from a Seaglider mission north of O‘ahu to examine
434 the subsurface temperature fields from the EXNF and EXF experiments. In the initial

cycle, the mean temperature profile from the observations matches the mean profile from both EXNF and EXF; however, after each subsequent cycle, EXNF is increasingly colder than the observations. This is most apparent in depths from 140 m to 220 m, where a cool 1.5 K bias first develops, then increases to more than 3 K from 40 m to 200 m in the final cycle of the experiment. This is accompanied with an increase in RMSE above 200 m depth in the EXNF experiment that is not found in EXF. In the EXF experiment, a minor increase is found in RMSE of less than 0.5 K in the 4th and 6th cycle, but no change above 200 m exists. This is a similar pattern to that found in the NF08 experiment, with an increase in temperature bias and RMSE at the 40–160 m layer.

3.6. Impact of assimilation on mixed layer depths

We have shown that the assimilation of SST observations without surface forcing adjustment affects the subsurface structure of temperature in the model; however, the largest effects have been limited to depths below 40 m. We explore the effects of the assimilation on the mixed layer depth (MLD) in this section. A cold bias exists in the NF08 experiment at depths between 40 m and 200 m that suggest colder waters are shoaled. F09M/W should have less impact upon the MLD as the atmospheric forcing adjustment provides the means to match the SST. We calculate the MLD using the finite difference criteria method from a near-surface reference depth of 10 m. We use a 0.2°C temperature difference as the criterion to define the MLD, as suggested by de Boyer Montégut et al. [2004]. This method and temperature criterion are also used to generate MLD climatologies from the Asia-Pacific Data-Research Center (APDRC) that are compared with the results from FWD, NF08, F09M, and F09W. The MLD climatology is made a regular 2° by 2° grid

456 for every month and was generated from over 60 years of high vertical resolution profiling
457 data.

458 The MLD climatology shows a seasonal variation that ranges from less than 40 m in
459 April to more than 75 m in November. The seasonal signal is suppressed near the island
460 and the MLD is shoaled as compared to abyssal waters. Figure 7a shows the spatially and
461 temporally averaged MLD values per cycle for abyssal waters from the climatology and
462 experiments, while Figure 7b shows the spatially averaged values for near island waters.
463 The experiments capture the seasonal signal in both abyssal waters and coastal/leeward
464 waters, though is deeper in the winter and shallower in summer. The largest reductions
465 in MLD are in the NEC, where the F09M and F09W MLD is more than 30 m shallower
466 than those from the FWD experiment. Spatially averaged MLDs from F09 cases shown
467 in Figures 7a and 7b demonstrate a similar seasonal pattern to that found in climatology
468 and the FWD experiment. Overall, the MLD from the assimilation experiments better
469 matches the climatological MLD with the FWD MLD extending too deep during the
470 winter months.

3.7. Impact of assimilation on tidal energy

471 It is not possible for a model to perfectly reproduce the tidal dynamics of the observa-
472 tions in regions where barotropic tides interact strongly with the topography and generate
473 baroclinic tides. This is because of the differing bathymetric representation of a model, as
474 well as the pseudo-random phase shifts in the baroclinic tides due to density variations.
475 To assimilate SSH observations one must remove their tidal signal, then add back tidal
476 information from the model. We explore the effects of the assimilation adjustments to
477 both the barotropic and baroclinic tidal dynamics in this section. The assimilation system

478 was not configured to improve the tidal flow directly; however, relatively small changes
479 should be seen if the system is working correctly.

480 To examine possible effects of the assimilation on the spatial structure of the surface
481 expression of the tides we focus on the dominant semidiurnal (M_2) tide, calculating the
482 phases and amplitudes from the four experiments. The internal tides reflect off of the
483 surface; hence, the free-surface does not provide a purely barotropic tidal signal. Figures
484 8a and 8b show the changes in amplitude and phase made during the NF08 and F09M as-
485 similation experiments. The changes in phase due to the assimilation are negligible in the
486 eastern half of the domain. This is to be expected, as the baroclinic energy flux emanates
487 South-Southwest from Kaena Ridge and South from French Frigate Shoals [Rainville et al.,
488 2010]. In these directions, extending from the islands of O‘ahu and Kaua‘i, the baroclinic
489 tides are shifted in phase during the assimilation by as much as 5° (over 10 minutes) and
490 in amplitude by 1 cm (10–20% of the M_2 amplitude) due to variations in the vertical
491 density structure and mesoscale currents in the analysis.

492 We generate time-series of surface baroclinic zonal velocities by subtracting the depth-
493 averaged velocity from the surface current and – in the case of the assimilation experiments
494 – omit the initial increments to analyze the baroclinic spectrum for each experiment. Space
495 averaged power spectral density (PSD) from the time series generated from FWD, NF08
496 and FA9(M/W) experiments all contain narrow-band peaks in energy at the S_2/M_2 , N_2 ,
497 S_1 , K_1 , and O_1 frequencies (Figure 9); however, with slightly different energy levels. The
498 PSDs show a transfer of energy from the tidal frequencies to the surrounding harmonics
499 due to changes in the stratification made during the assimilation that are not present in
500 the FWD experiment. Varying stratification associated with mesoscale currents impacts

501 the propagation of internal tides [Park and Watts, 2006] and the resulting phase and
502 amplitude modulation smears the energy out of phase-locked signals [Chavanne et al.,
503 2010]. This transfer of energy is highest in the NF08 run where, as previously discussed,
504 greater increments are made to the density field.

3.8. Impact of assimilation on inertial energy

505 Figure 9 reveals significant increases in energy levels in assimilation experiments from
506 20–48 hours that peak in the inertial period range for the domain (29–41 hours for the
507 region). The amplitudes of these oscillations are an order of magnitude larger in assimi-
508 lation experiments, when compared to FWD, and vary in period latitudinally consistent
509 with inertial motions. PSDs of the free-surface and depth averaged velocities from as-
510 similation experiments show no increase in energy in this period range, when compared
511 to FWD, suggesting the oscillations are purely baroclinic. Such spurious inertial oscil-
512 lations have been reported in both meteorological [Polavarapu et al., 2000] and oceanic
513 [Lea et al., 2006] variational data assimilation studies and are associated with ageostrophic
514 imbalances in the initial conditions from the IS4D-Var increment.

515 The PSDs shown in Figure 9 clearly demonstrate that there are strong oscillations
516 in inertial periods in the assimilation experiments, however, they provide little insight
517 into the behavior or generation mechanisms. We must use non-Fourier based analysis
518 to estimate the localized phase and amplitude of the oscillations because of the discrete
519 signal change after each assimilation cycle. The continuous wavelet transform (CWT)
520 has been shown to be useful in capturing non-stationary high-frequency signals in the
521 ocean [Flinchem and Jay, 2000], giving the evolution of signal characteristics through the
522 data set. Figure 10a shows a representative time-series of surface zonal velocities from

523 a single point in the center of the domain from both the FWD and NF08 experiments.
524 We ensure that any increase in inertial oscillations are not generated by adjustments to
525 wind stress possible in the FA09M/W experiments by using a time series from the NF08
526 experiment. Figures 10b and 10c show wavelet scalograms from 10th order Gaussian CWT
527 of the FWD and NF08 surface zonal velocity time-series. The Gaussian wavelet is chosen
528 because of its flexibility in time and frequency resolution. In the FWD wavelet scalogram
529 there is a continuity of energy at 12 hours and 24 hours from the semi and diurnal tidal
530 constituents, along with intermittent increases in wave amplitudes around inertial periods
531 having maximum values of 35 cm/s. Similar energy at the diurnal and semidiurnal tidal
532 periods is present in the scalogram from the NF08 time series, however, at inertial periods
533 in the NF08 scalogram wave amplitudes close to 75 cm/s are common. The variability in
534 the NF08 time series is much larger than FWD, with a standard deviation of over 23 cm/s,
535 compared to 14 cm/s in the FWD case, and the scalograms suggest that the increased
536 variability is focused in the inertial spectral band.

537 Comparing CWT scalograms generated from surface velocity time series from other
538 parts of the domain in the NF08, F09M, and F09W experiments suggests that spurious
539 inertial oscillations are commonly generated during the assimilation using both configu-
540 rations. However, the spurious inertial oscillations are significantly damped in shallow
541 waters near the island chain. The timing and locations of the increases in inertial wave
542 amplitudes suggests that the spurious oscillations are associated with large increments ap-
543 plied at the surface in response to assimilating either SSH or SST observations. To verify
544 this we conducted an additional experiment that assimilated only SSH or SST data, and
545 found spurious inertial oscillations in both cases. Also, in this short test, from assimilating

546 SST only the oscillations were more pronounced than when compared to assimilating SSH
547 only.

548 In future assimilation experiments, the balanced initialization feature within ROMS
549 could be used to limit the generation of spurious inertial oscillations in the assimilation
550 experiments. The balance operator algorithm follows the methodology of Weaver and
551 Courtier [2001] to constrain the error covariance by establishing linear, geostrophically
552 balanced relationships between state variables. However, it utilizes an elliptical solver
553 that may limit its effectiveness in an island domain. Also, because any discrete change to
554 a continuous system will radiate energy, to fully dampen the spurious inertial oscillations
555 requires a digital filter as has been shown in numerical weather prediction, such as that
556 described in Polavarapu et al. [2000].

3.9. Impact of assimilation on low-frequency dynamics

557 We examine the impact of high-frequency variability added to the assimilation exper-
558 iments via inertial oscillations on the low-frequency eddy kinetic energy (EKE) in the
559 NF08, F09M, and F09W experiments in this section. EKEs are calculated from the av-
560 erage surface velocity fields of each four-day experiment cycle to filter out tides, inertial
561 oscillations, and other high-frequency signals. We then compare our results with EKE
562 estimates from the AVISO weekly mapped absolute geostrophic current (AGC) product.
563 The AGC fields are generated by optimally interpolating along-track altimetry data and
564 represent only geostrophic velocity, hence, the EKE from AGC should underestimate the
565 true variability in the ocean. Figure 11a shows the spatially averaged EKE per experiment
566 cycle from FWD and assimilation cases along with the average EKE from AGC over the
567 entire domain. EKE values from AGC show no trend, maintaining a constant value of

568 100 (cm/s)². FWD EKE agrees in magnitude with that from AGC until the change to
569 WRF forcing in late July 2009. Eddies formed in lee of the Hawai‘i dramatically increase
570 EKE, because of this, we also show mean EKE from in lee of Hawai‘i to 158.5° W (Figure
571 11b). EKE values from AGC in lee of Hawai‘i vary in time, ranging from 100–600 (cm/s)².
572 FWD case EKE values, in the leeward region, when using MM5/NCEP forcing are less
573 than those from AGC. This suggests that the non-linear model is underestimating the
574 EKE when forced by MM5/NCEP fields. Average EKE values from the entire domain in-
575 creases gradually to more than double those from AGC after the change to WRF forcing,
576 and in lee to more than 6 times those from AGC.

577 After the first few cycles, average EKE values for the entire domain in assimilation
578 experiments range between 200 (cm/s)² and 400 (cm/s)², 2–4 times more than EKE
579 values from AGC. In assimilation experiments the increase in leeward EKE, relative to the
580 domain average, compares well with the leeward increase from AGC. EKE values over the
581 entire domain from the NF08 experiment are slightly larger than those from F09M/F09W.
582 Leeward EKE values in the NF08 experiment spike to over 900 (cm/s)². These increases
583 are not present in the F09M and F09W experiments and are likely due to increased
584 variability generated in the model via the increment in the NF08 experiment. Also, the
585 large increase in EKE in the FWD experiment, after the change to WRF forcing, is not
586 seen in assimilation experiments, as EKE values maintain a range of 200–300 (cm/s)² over
587 the domain and 400–700 (cm/s)² in lee during this time period. The EKE levels from
588 assimilation experiments agree well with estimates from eddy-resolving ocean general
589 circulation models [Noh et al., 2007].

4. Conclusions

We have explored the behavior of a four-dimensional variational data assimilation system applied to the Hawaiian Island region by using two assimilation configurations, with and without surface forcing adjustment, and two atmospheric forcing products, a combination of NCEP/MM5 and WRF. All available observations were assimilated including satellite altimetry and radiometry, and *in situ* temperature and salinity profiles collected from autonomous Seagliders, Argo floats, and shipboard CTD. We found significant reductions in misfit RMSE are made between the model and SST (23–51%) and salinity (29–47%) observations, when compared against a control run without data assimilation, from both assimilation configurations, using either atmospheric forcing product. The RMSE between all assimilation experiments and SST observations approached the average observational error of 0.31 K, except in lee of Hawai‘i, where reduced horizontal decorrelation length scales, as well as increased variability limited the reduction of RMSE to 0.6 K. Improvements in RMSE with regard to the high-resolution, along-track SSH observations were limited to 13–14% because of underestimated SSH observational error and the inclusion of tidal signals when calculating the prior background covariance. The use of low-resolution, real-time, along-track data further limited the reductions of SSH RMSE within the assimilation to less than 4%.

The configuration of the assimilation system had a large effect on the subsurface temperature structure. Reductions of RMSE, compared against the control run, between the model and *in situ* temperature observations were limited to 6% when adjusting only initial conditions. These reductions in RMSE improved to 28% if atmospheric forcing was also adjusted during assimilation. This was due to the inability of the assimilation system to

respond to diurnal biases between the modeled and observed SST without atmospheric adjustments in time. The assimilation system degrades the temperature structure in the interior of the ocean by unrealistically cooling waters below the mixed layer (from 40 m to 200 m) if only initial conditions were adjusted. The depth of the mixed layer was slightly shoaled during the assimilation using both configurations, however, showed better agreement with climatology in the region, compared to the control run without data assimilation. When atmospheric forcing was also adjusted during the assimilation procedure there was no evidence of incorrect sub-surface cooling, as the adjustment of heat flux in time was able to account for diurnal SST biases. Along with heat flux, there were salt flux and wind stress adjustments during the assimilation; however, only relatively small changes were made.

Baroclinic tides in the analysis were modified during assimilation by 10–20% in amplitude and over 10 minutes in phase in regions where internal tide generation occurs. The modifications were due to changes in the density structure that affected the surface expression of the baroclinic tides. The overall energies of surface baroclinic tides were minimally affected during the assimilation, however, some small transfer of energy from tidal frequencies to surrounding harmonics were found at semi and diurnal bands.

Significant spurious inertial oscillations were found in assimilation dynamics due to imbalances in initial conditions from the IS4D-Var increment. These oscillations were associated with the assimilation of both, or either, SSH and SST observations. However, these oscillations found in assimilation fields showed little effect on the low-frequency variability. The overall flow of the region was maintained and an improvement to the EKE in the immediate lee of the island of Hawai'i was achieved. This increase in EKE

635 better reflected the generation of eddies that shed in the lee of the island; however, the
636 assimilation increased the EKE over the entire domain to more than is observed.

637 We have shown that over four-day period, IS4D-Var is effective at sub-mesoscale reso-
638 lution in the presence of strong barotropic flow with significant energy conversion into the
639 baroclinic tides. The assimilation was able to balance a majority of SST observations with
640 a limited set of *in situ* observations that captured these baroclinic tides. Amidst these
641 processes, the results show that over a wide variety of dynamical length- and time-scales,
642 the 4D-Var solution is consistent with the observations.

643 **Acknowledgments.**

644 We wish to thank the editor and two anonymous reviewers for improving this
645 manuscript. Dr. Matthews was supported by NOAA Grant #NA07NOS4730207, Dr.
646 Powell was supported by The Office of Naval Research Grant #N00014-09-10939, and Dr.
647 Janeković was supported on NOAA grant #NA10NOS4730016. The authors would also
648 like to thank Prof. Glenn Cater for providing Seaglider observational data and Prof. Roger
649 Lukas for providing Hawai'i Ocean Time-series observations, which are supported by the
650 U.S. National Science Foundation under Grant OCE-0327513. This SOEST publication
651 #8529.

References

- 652 Akima, 1984. On estimating partial derivatives for bivariate interpolation of scattered
653 data. Rocky Mountain Journal of Mathematics, 41–52.
- 654 Barron, C. N., Kara, C. A., Martin, P. J., Rhodes, R. C., Smedstad, L. F., 2006. For-
655 mulation, implementation and examination of vertical coordinate choices in the Global

- 656 Navy Coastal Ocean Model (NCOM). *Ocean Modelling* 11, 347–375.
- 657 Broquet, G., Edwards, C. A., Moore, A., Powell, B. S., Veneziani, M., Doyle, J. D.,
658 2009. Application of 4D-Variational data assimilation to the California Current System.
659 *Dynam. Atmos. Oceans* 48, 69–92.
- 660 Broquet, G., Moore, A. M., Arango, H. G., Edwards, C. A., 2011. Corrections to ocean
661 surface forcing in the California Current System using 4D variational data assimilation.
662 *Ocean Modelling* 36, 116–132.
- 663 Calil, P. H., Richards, K. J., Jia, Y., Bidigare, R. R., 2008. Eddy activity in the lee of the
664 Hawaiian Islands. *Deep-Sea Res., Part II* 55, 1,179–1,194.
- 665 Carter, G. S., Merrifield, M. A., Becker, J. M., Katsumata, K., Gregg, M. C., Luther,
666 D. S., Levine, M. D., Boyd, T. J., Firing, Y. L., 2008. Energetics of M_2 Barotropic-to-
667 Baroclinic Tidal Conversion at the Hawaiian Islands. *J. Phys. Oceanogr.* 38, 2,205–2,223.
- 668 Chapman, D. C., Aug. 1985. Numerical Treatment of Cross-Shelf Open Boundaries in a
669 Barotropic Coastal Ocean Model. *Journal of Physical Oceanography* 15, 1060–1075.
- 670 Chavanne, C., Flament, P., Carter, G., Merrifield, M. A., S.Luther, D., 2010. The sur-
671 face expression of semidiurnal internal tides near a strong source at Hawaii. Part I:
672 Observations and numerical predictions. *J. Phys. Oceanogr.* 40, 1155–1179.
- 673 Chen, S. M., Qiu, B., 2010. Mesoscale eddies northeast of the Hawaiian archipelago from
674 satellite altimeter observations. *J. Phys. Oceanogr.*
- 675 Chiswell, S. M., 1994. Vertical Structure of the Baroclinic Tides in the Central North
676 Pacific Subtropical Gyre. *Journal of Physical Oceanography* 24, 2032.
- 677 Clauss, E., Hinzpeter, H., Muller-Glewe, J., 1970. Measurements of the tempera-
678 ture structure in the water at the interface between the ocean-atmosphere. *Meteor*

- 679 Forschungsergeb B 5, 90–94.
- 680 Courtier, P., Thépaut, J. N., Hollingsworth, A., 1994. A strategy for operational im-
681 plementation of 4D-Var, using an incremental approach. *Q. J. R. Meteorol. Soc* 120,
682 1367–1387.
- 683 de Boyer Montégut, C., Madec, G., Fischer, A. S., Lazar, A., Iudicone, D., 2004. Mixed
684 layer depth over the global ocean: An examination of profile data and a profile-based
685 climatology. *Journal of Geophysical Research (Oceans)* 109, C12003.
- 686 Desroziers, G., Berre, L., Chabot, V., Chapnik, B., 2009. A Posteriori Diagnostics in an
687 Ensemble of Perturbed Analyses. *Mon. Weather Rev.* 137, 3,420–3,436.
- 688 Egbert, G. D., Bennett, A. F., Foreman, M. G. G., Dec. 1994. TOPEX/POSEIDON tides
689 estimated using a global inverse model. *J. Geophys. Res.*, 992, 24821–24852.
- 690 Fairall, C. W., Bradley, E. F., Rogers, D. P., Edson, J. B., Young, G. S., 1996. Bulk
691 parameterization of air-sea fluxes for tropical ocean–global atmosphere Coupled-Ocean
692 Atmosphere Response Experiment. *J. Geophys. Res.* 101, 3747–3764.
- 693 Fisher, M., 1998. Minimization Algorithms for Variational Data Assimilation. In: Seminar
694 on Recent Developments in Numerical Methods for Atmospheric Modelling. ECMWF.
- 695 Flament, P., Kennan, S., Lumpkin, R., Sawyer, M., Stroup, E., 1998. The ocean atlas of
696 hawaii. University of Hawaii Press.
- 697 Flinchem, E. P., Jay, D. A., 2000. An introduction to wavelet transform tidal analysis
698 methods. *Estuarine, Coastal and Shelf Science* 51 (2), 177 – 200.
- 699 Gentemann, C. L., Minnett, P. J., Ward, B., Jul. 2009. Profiles of ocean surface heating
700 (POSH): A new model of upper ocean diurnal warming. *Journal of Geophysical Research*
701 (Oceans) 114, 7017.

- 702 Grassl, H., 1976. A new type of absorption in the atmospheric infrared window due to
703 water vapor polymers. Beitraege zur Physik der Atmosphaere, vol. 49, no. 4, 1976,
704 p. 225-236. 49, 225–236.
- 705 Karl, D. M., Lukas, R., 1996. The Hawaii Ocean Time-Series (HOT) program: Back-
706 ground, rationale and field implementation. Deep-Sea Res., Part II 43, 129–156.
- 707 Large, W. G., McWilliams, J. C., Doney, S. C., 1994. Oceanic vertical mixing: a review
708 and a model with a nonlocal boundary layer parameterization. Reviews of Geophysics
709 32, 363–404.
- 710 Lea, D. J., Haine, T. W. N., Gasparovic, R. F., 2006. Observability of the irminger sea
711 circulation using variational data assimilation. Quarterly Journal of the Royal Meteorological Society 132 (618), 1545–1576.
- 712 Liu, W. T., Businger, J. A., Sep. 1975. Temperature Profile in the Molecular Sublayer
713 Near the Interface of a Fluid in Turbulent Motion. *Geophys. Res. Lett.*, 2, 403–404.
- 714 Lorenc, A., 2006. Why does 4D-Var beat 3D-Var? Q. J. R. Meteorol. Soc 131, 3,247–3,257.
- 715 Lumpkin, C., 1998. Eddies and currents of the hawaiian islands. PhD. Dissertation -
716 School of Ocean and Earth Science, University of Hawaii at Manoa.
- 717 Marchesiello, P., 2001. Open boundary conditions for long-term integration of regional
718 oceanic models. Ocean Modelling 3, 1–20.
- 719 Matthews, D., Powell, B., Milliff, R., 2011. Dominant spatial variability scales from obser-
720 vations around the hawaiian islands. Deep Sea Research Part I: Oceanographic Research
721 Papers 58 (10), 979 – 987.
- 722 McClain, E. P., Pichel, W. G., Walton, C. C., Nov. 1985. Comparative performance of
723 AVHRR-based multichannel sea surface temperatures. *J. Geophys. Res.*, 901, 11587–

- 725 11601.
- 726 Merrifield, M. A., Holloway, P. E., Johnston, T. M. S., Feb. 2001. The generation of
727 internal tides at the Hawaiian Ridge. *Geophys. Res. Lett.*, 28, 559–562.
- 728 Milliff, R. F., Morzel, J., Chelton, D. B., Freilich, M. H., 2004. Wind Stress Curl and
729 Wind Stress Divergence Biases from Rain Effects on QSCAT Surface Wind Retrievals.
730 Journal of Atmospheric and Oceanic Technology 21, 1216.
- 731 Moore, A. M., Arango, H. G., Broquet, G., Edwards, C., Veneziani, M., Powell, B. S.,
732 Foley, D., Doyle, J., Costa, D., Robinson, P., 2011a. The Regional Ocean Modeling
733 System (ROMS) 4-dimensional variational data assimilation systems: Part II – Perfor-
734 mance and application to the California Current System. *Prog. Oceanog.* 91, 50–73.
- 735 Moore, A. M., Arango, H. G., Broquet, G., Edwards, C., Veneziani, M., Powell, B. S.,
736 Foley, D., Doyle, J., Costa, D., Robinson, P., 2011b. The Regional Ocean Modeling
737 System (ROMS) 4-dimensional variational data assimilation systems: Part III – Ob-
738 servation impact and observation sensitivity in the California Current System. *Prog.*
739 *Oceanog.* 91, 74–94.
- 740 Moore, A. M., Arango, H. G., Broquet, G., Powell, B. S., Zavala-Garay, J., Weaver, A. T.,
741 2011c. The Regional Ocean Modeling System (ROMS) 4-dimensional variational data
742 assimilation systems: Part I – System overview and formulation. *Prog. Oceanog.* 91,
743 34–49.
- 744 Moore, A. M., Arango, H. G., Lorenzo, E. D., Cornuelle, B. D., Miller, A. J., Neilson,
745 D. J., 2004. A comprehensive ocean prediction and analysis system based on the tangent
746 linear and adjoint of a regional ocean model. *Ocean Modelling* 7, 227–258.

- 747 Noh, Y., Yim, B. Y., You, S. H., Yoon, J. H., Qiu, B., Apr. 2007. Seasonal variation of
748 eddy kinetic energy of the North Pacific Subtropical Countercurrent simulated by an
749 eddy-resolving OGCM. *Geophys. Res. Lett.*, 340, L07601.
- 750 Oka, E., Ando, K., 2004. Stability of temperature and conductivity sensors of argo profiling
751 floats. *Journal of Oceanography* 60 (2), 253–258.
- 752 Park, J.-H., Watts, D. R., 2006. Internal Tides in the Southwestern Japan/East Sea.
753 *Journal of Physical Oceanography* 36, 22–+.
- 754 Polavarapu, S., Tanguay, M., Fillion, L., 2000. Four-Dimensional Variational Data Assim-
755 ilation with Digital Filter Initialization. *Monthly Weather Review* 128, 2491–+.
- 756 Powell, B. S., Arango, H. G., Moore, A. M., Di Lorenzo, E., Milliff, R. F., Foley, D.,
757 2008. 4DVAR Data Assimilation in the Intra-Americas Sea with the Regional Ocean
758 Modeling System (ROMS). *Ocean Modelling* 25, 173–188.
- 759 Powell, B. S., Moore, A. M., Arango, H. G., Milliff, R. F., Leben, R. R., 2009. Real-
760 Time Assimilation and Prediction in the Intra-Americas Sea with the Regional Ocean
761 Modeling System (ROMS). *Dyn. Atmos. Oceans* 48, 46–68.
- 762 Rainville, L., Johnston, T. M. S., Carter, G. S., Merrifield, M. A., Pinkel, R., Worcester,
763 P. F., Dushaw, B. D., 2010. Interference Pattern and Propagation of the M_2 Internal
764 Tide South of the Hawaiian Ridge. *J. Phys. Oceanogr.* 40, 311–325.
- 765 Ray, R. D., Mitchum, G. T., 1996. Surface manifestation of internal tides generated near
766 Hawaii. *Geophys. Res. Lett.*, 23, 2101–2104.
- 767 Robinson, I. S., Wells, N. S., Charnock, H., 1984. The sea surface thermal boundary
768 layer and its relevance to the measurement of sea surface temperature by airborne and
769 spaceborne radiometers. *International Journal of Remote Sensing* (ISSN 0143-1161),

770 vol. 5 vol. 5.

771 Schluessel, P., Emery, W. J., Grassl, H., Mammen, T., 1990. On the bulk-skin temperature
772 difference and its impact on satellite remote sensing of sea surface temperature. *J.*

773 *Geophys. Res.*, 951, 13341–13356.

774 Shchepetkin, A. F., McWilliams, J. C., 2005. The Regional Oceanic Modeling System: A
775 split-explicit, free-surface, topography-following-coordinate ocean model. *Ocean Mod-*
776 *elling* 9, 347–404.

777 Smith, R. B., Grubii, V., 1993. Aerial Observations of Hawaii's Wake. *Journal of Atmo-*
778 *spheric Sciences* 50, 3728–3750.

779 Talagrand, O., Courtier, P., 1987. Variational assimilation of meteorological observations
780 with the adjoint vorticity equation. I: Theory. *Q. J. R. Meteorol. Soc* 113, 1311–1328.

781 Weaver, A., Courtier, P., 2001. Correlation modelling on the sphere using generalized
782 diffusion equation. *Q. J. R. Meteorol. Soc* 127, 1815–1846.

783 Xie, S.-P., Liu, W., Liu, Q., Nonaka, M., 2001. Far-Reaching Effects of the Hawaiian
784 Islands on the Pacific Ocean-Atmosphere System. *Science* 292 (5524), 2057–2060.

785 Yang, Y., Chen, Y.-L., Fujioka, F. M., 2008a. Effects of Trade-Wind Strength and Direc-
786 tion on the Leeside Circulations and Rainfall of the Island of Hawaii. *Monthly Weather
787 Review* 136, 4799.

788 Yang, Y., Xie, S.-P., Hafner, J., Aug. 2008b. Cloud patterns lee of Hawaii Island: A
789 synthesis of satellite observations and numerical simulation. *Journal of Geophysical
790 Research (Atmospheres)* 113, D15126.

791 Yoshida, S., Qiu, B., Hacker, P., 2010. Wind generated eddy characteristics in the lee of
792 the island of Hawaii. *J. Geophys. Res.* 115.

- 793 Zanifé, O. Z., Vincent, P., Amarouche, L., Dumont, J. P., Thibaut, P., Labroue, S., 2003.
- 794 Comparison of the Ku-band range noise level and the relative sea-state bias of the
- 795 Jason-1, TOPEX, and Poseidon-1 radar altimeters. *Marine Geodesy*, 201–238.
- 796 Zhang, W. G., Wilkin, J. L., Arango, H. G., 2010. Towards an integrated observation and
- 797 modeling system in the New York Bight using variational methods. Part I: 4DVAR data
- 798 assimilation. *Ocean Modelling* 35, 119–133.

Table 1. Summary of numerical experiments used in the study.

Name	Description	Time Period
FWD	Forward model with no assimilation	January 1, 2008 – January 4, 2010
NF08	Assimilation, no forcing adjustment, forcing from MM5/NCEP	January 1, 2008 – January 1, 2009
F09M	Assimilation, forcing adjustment, forcing from MM5/NCEP	January 2, 2009 – July 16, 2009
F09W	Assimilation, forcing adjustment, forcing from WRF	July 16, 2009 – January 4, 2010

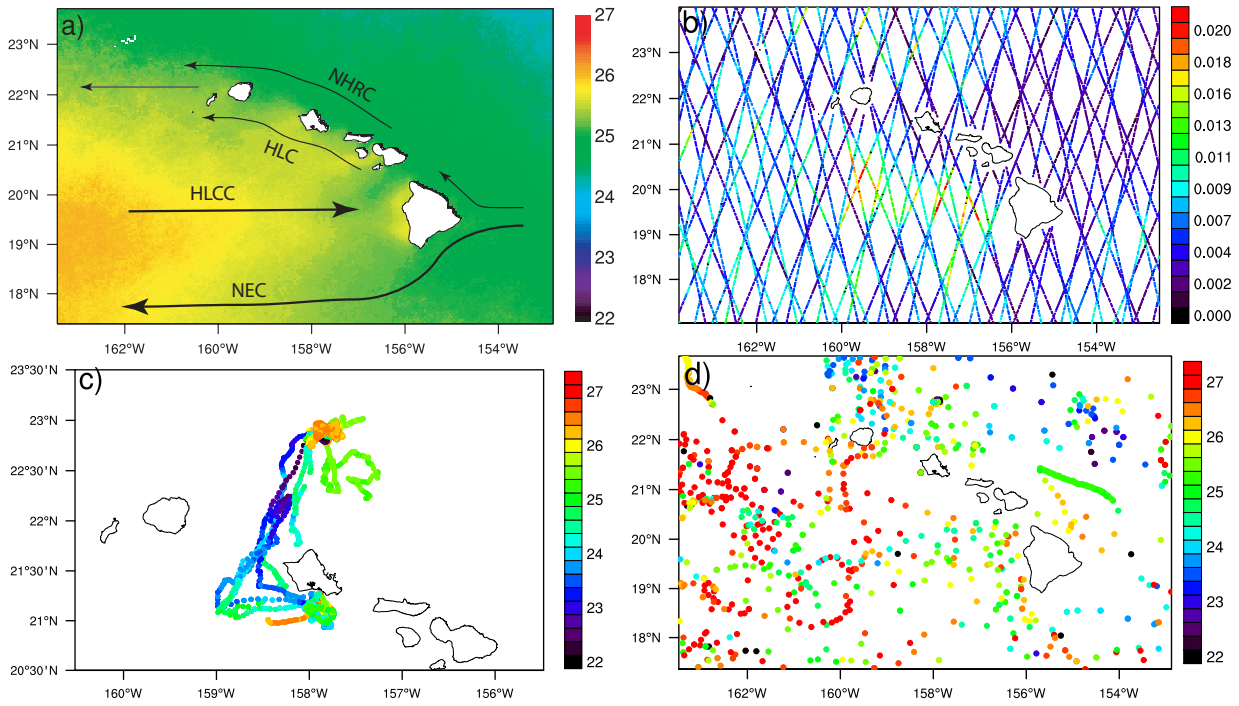


Figure 1. Time averaged map from satellite observations of SST at the model grid

(a) and temporal variance of SLA observations (b), temperatures above 20 m depth layer from Seagliders (c), and Argo and shipboard profiles (d).

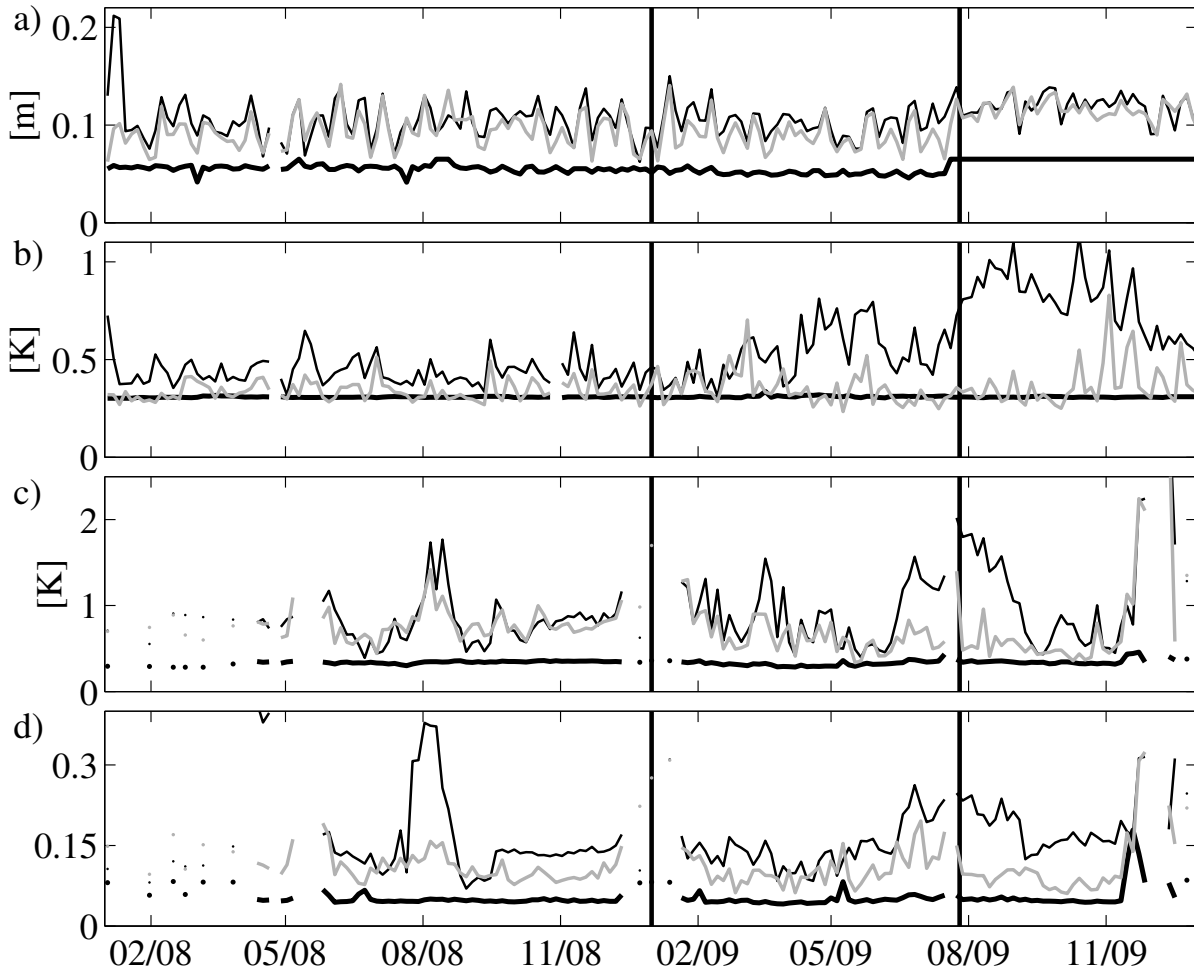


Figure 2. Time-series of RMSE between the model (FWD experiment shown by thin black line and NF08, F09M, and F09W shown with thin grey line) and observations (SSH (a), SST (b), temperature below surface (c), and salinity (d)) per experiment cycle. The mean observational error per cycle is shown by the thick dashed line. The time periods of the NF08, F09M, and F09W experiments are shown by the vertical lines.

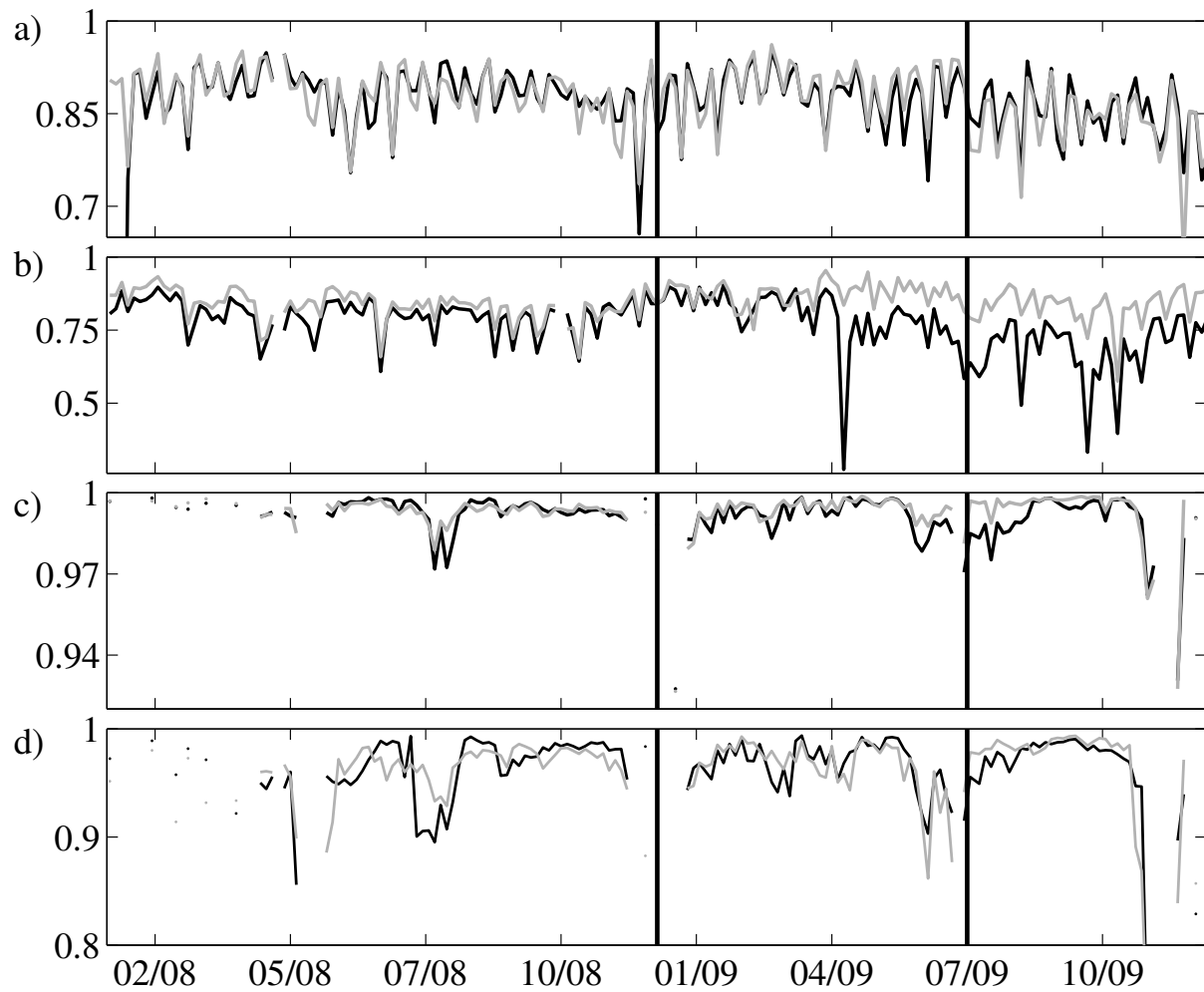


Figure 3. Correlation coefficients computed over each cycle between the model (FWD shown with black line and NF08, F09M, and F09W shown by grey lines) and observations for SSH (a), SST (b), subsurface temperature (c), and salinity (d). Vertical lines are similar to Figure 2.

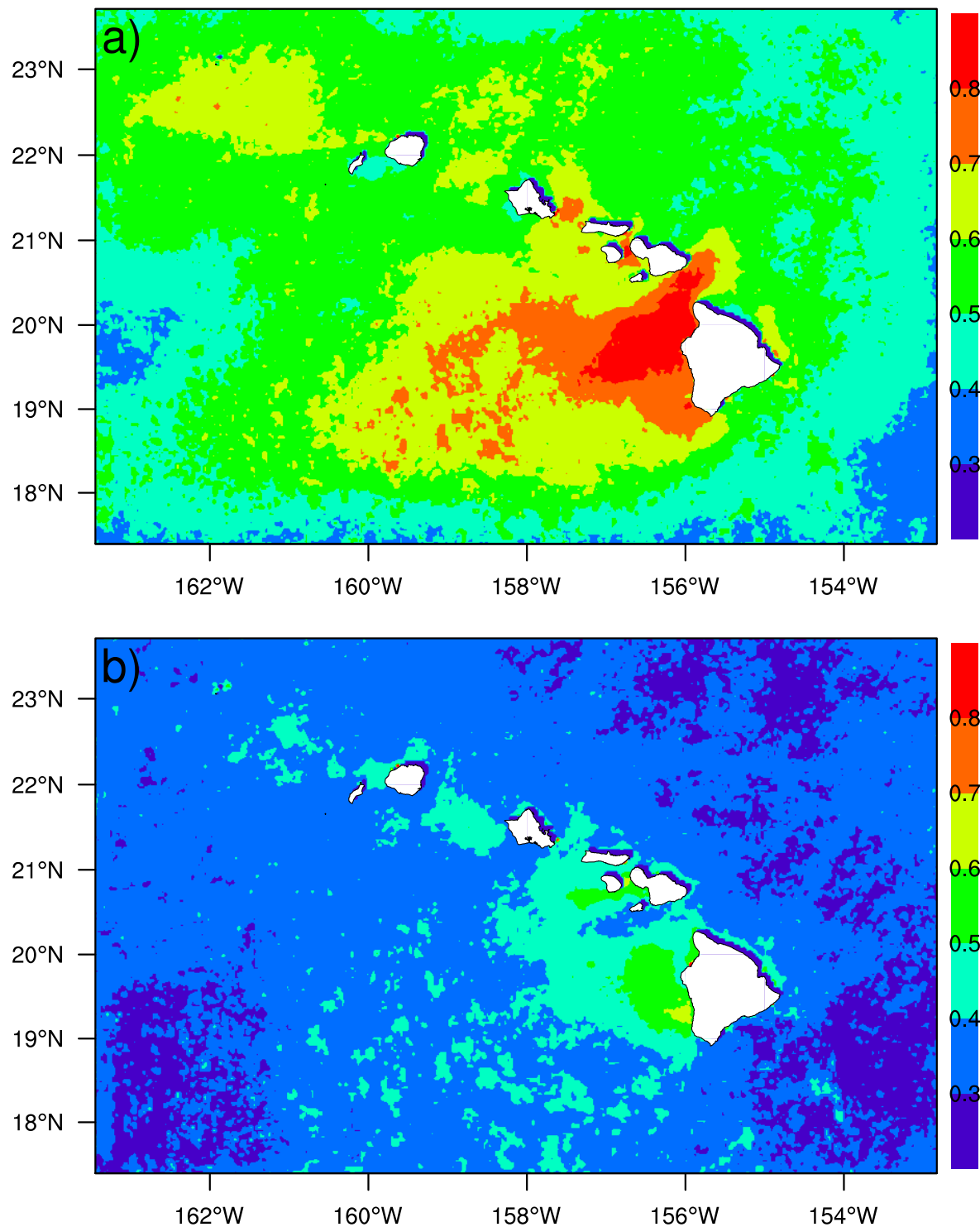


Figure 4. Time averaged SST RMSE [K] from FWD (a) and assimilation experiments (b) based on the two-year study period.

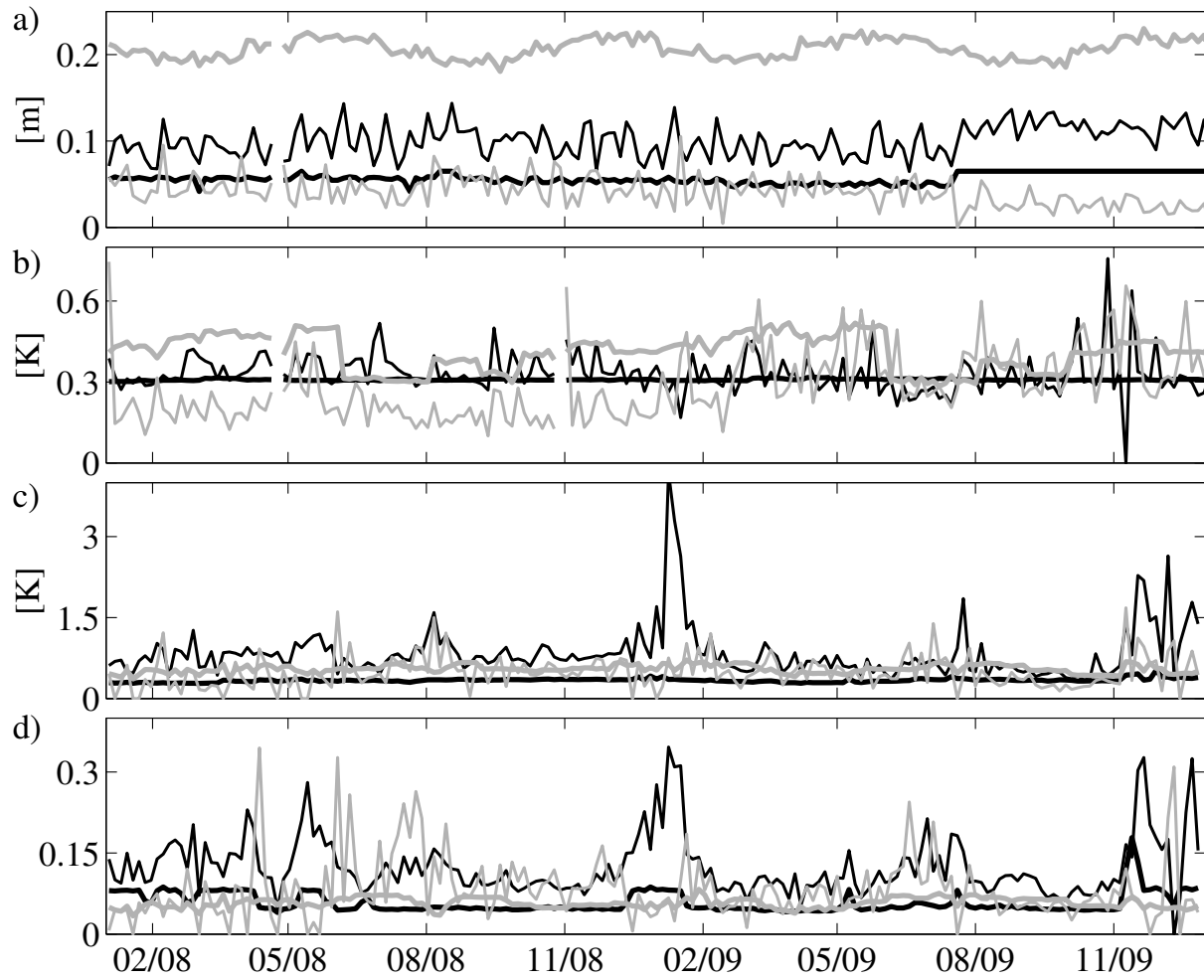


Figure 5. Time series of spatially averaged *a priori* background errors (grey thick line) and observation (black thick line) standard deviations. Time series of *posterior* background (grey thin line) and observation (black thin line) standard deviations computed from Eq. 3 and Eq. 4. Values are for SSH (a), SST (b), subsurface temperature (c), and salinity (d).

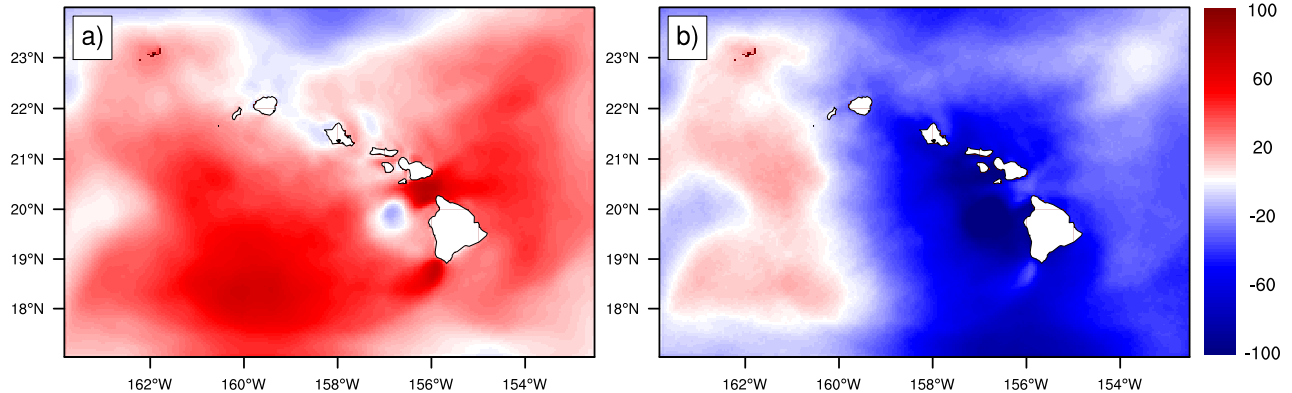


Figure 6. Time averaged heat flux [W/m^2] adjustments made during the F09M and F09W experiments at 2 PM (a) and 2 AM (b) local time.

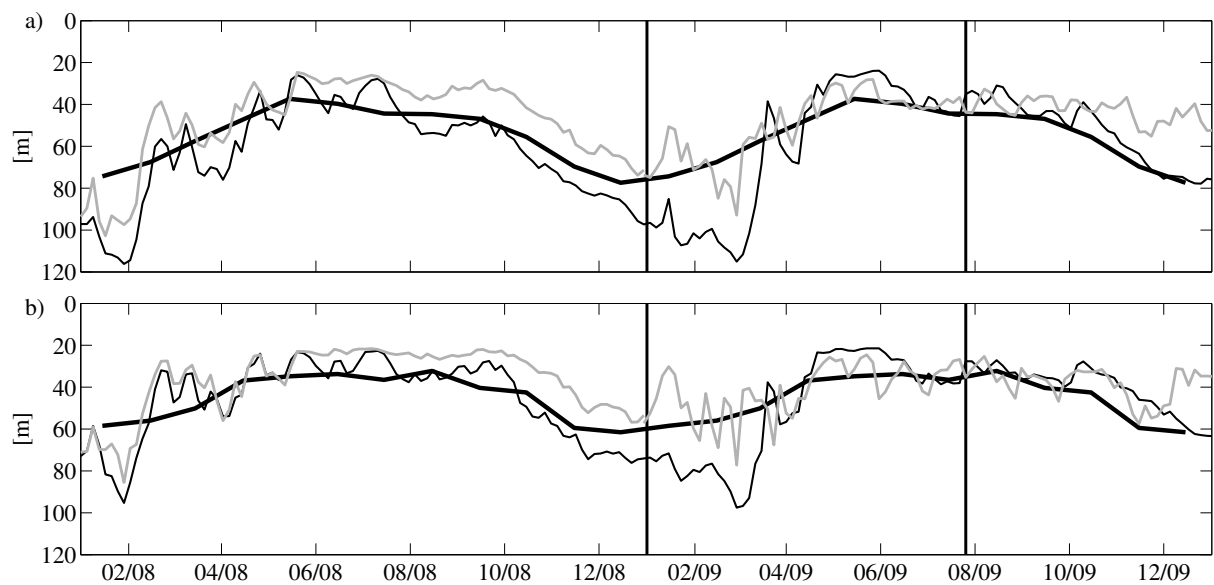


Figure 7. Mixed layer depths from abyssal waters (a) and leeward/coastal waters (b) from climatology (thick black line), the FWD experiment (thin black line), and the NF08/F09M/F09W experiments (thin grey line). Vertical lines are similar to Figure 2.

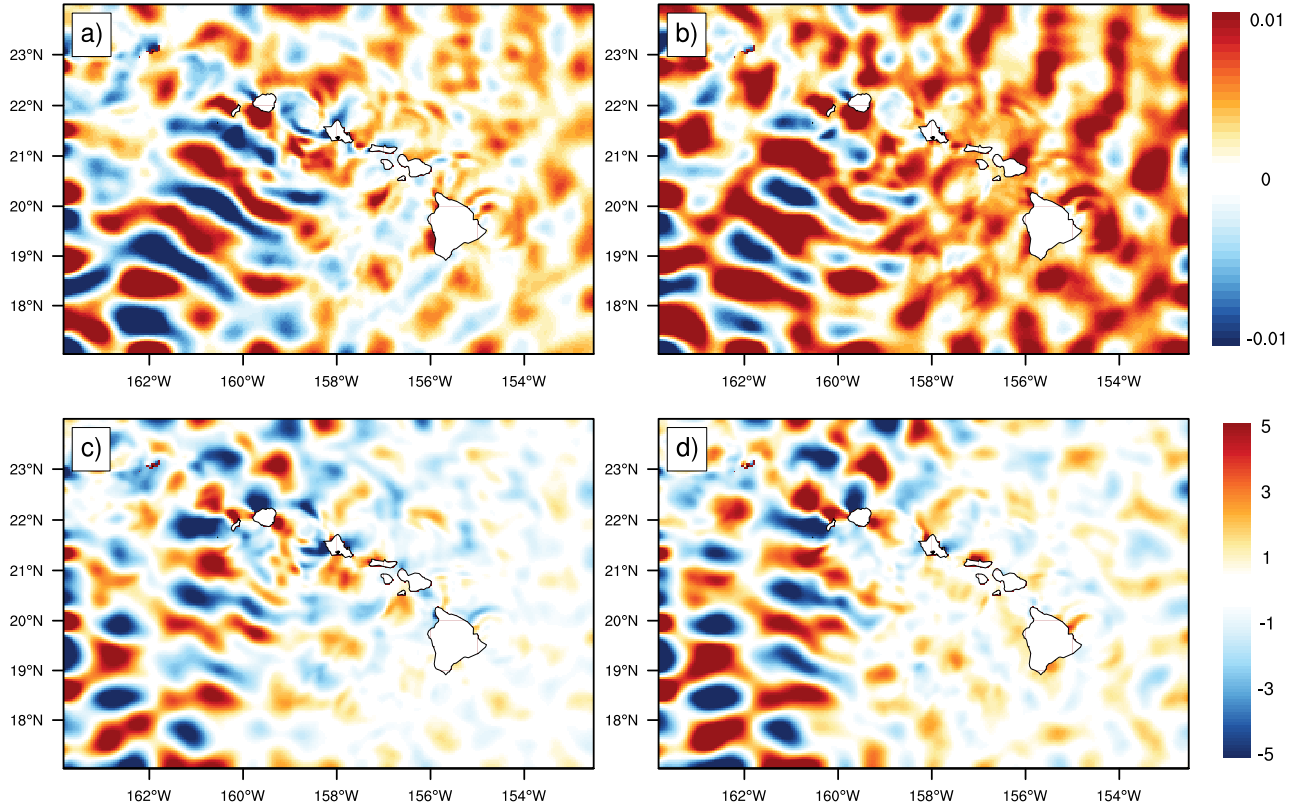


Figure 8. Time averaged M_2 tidal amplitude [m] and phase [°] differences between assimilation experiments, and the FWD case. [(a) amplitude difference (NF08–FWD), (b) phase difference (NF08–FWD), (c) amplitude difference (F09M/F09W–FWD) (d) phase difference (F09M/F09W–FWD)].

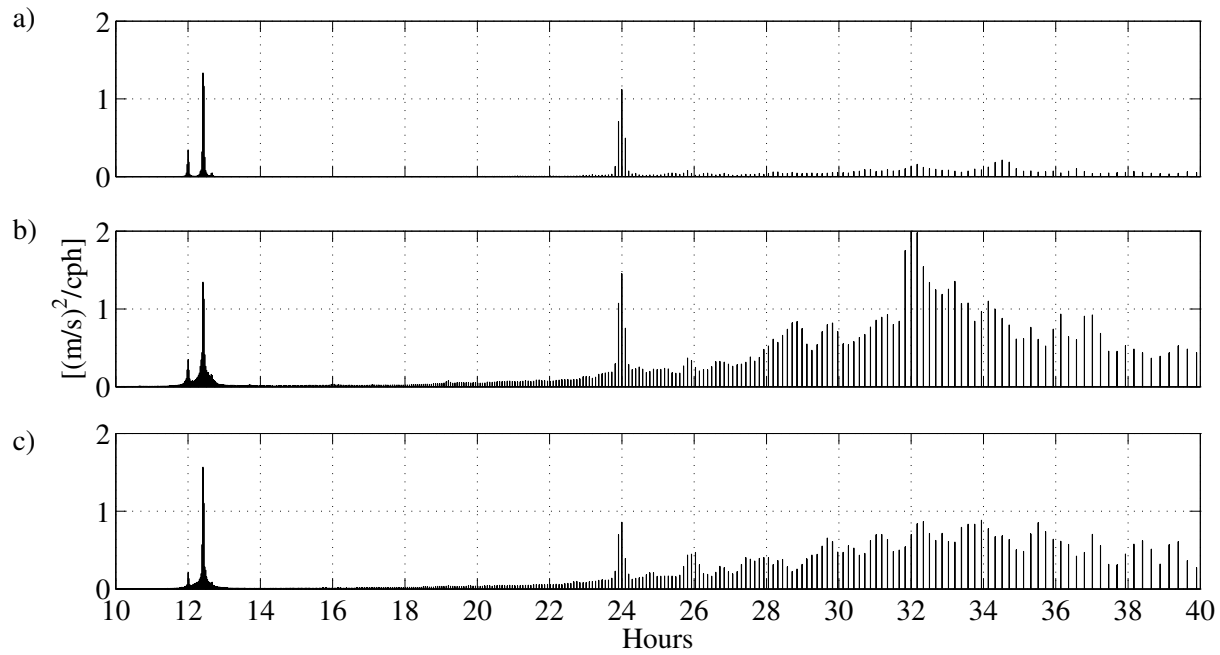


Figure 9. Spatially averaged power spectral density for time series of surface baroclinic zonal velocities in the FWD (a), NF08 (b) and the F09M/F09W (c) experiments.

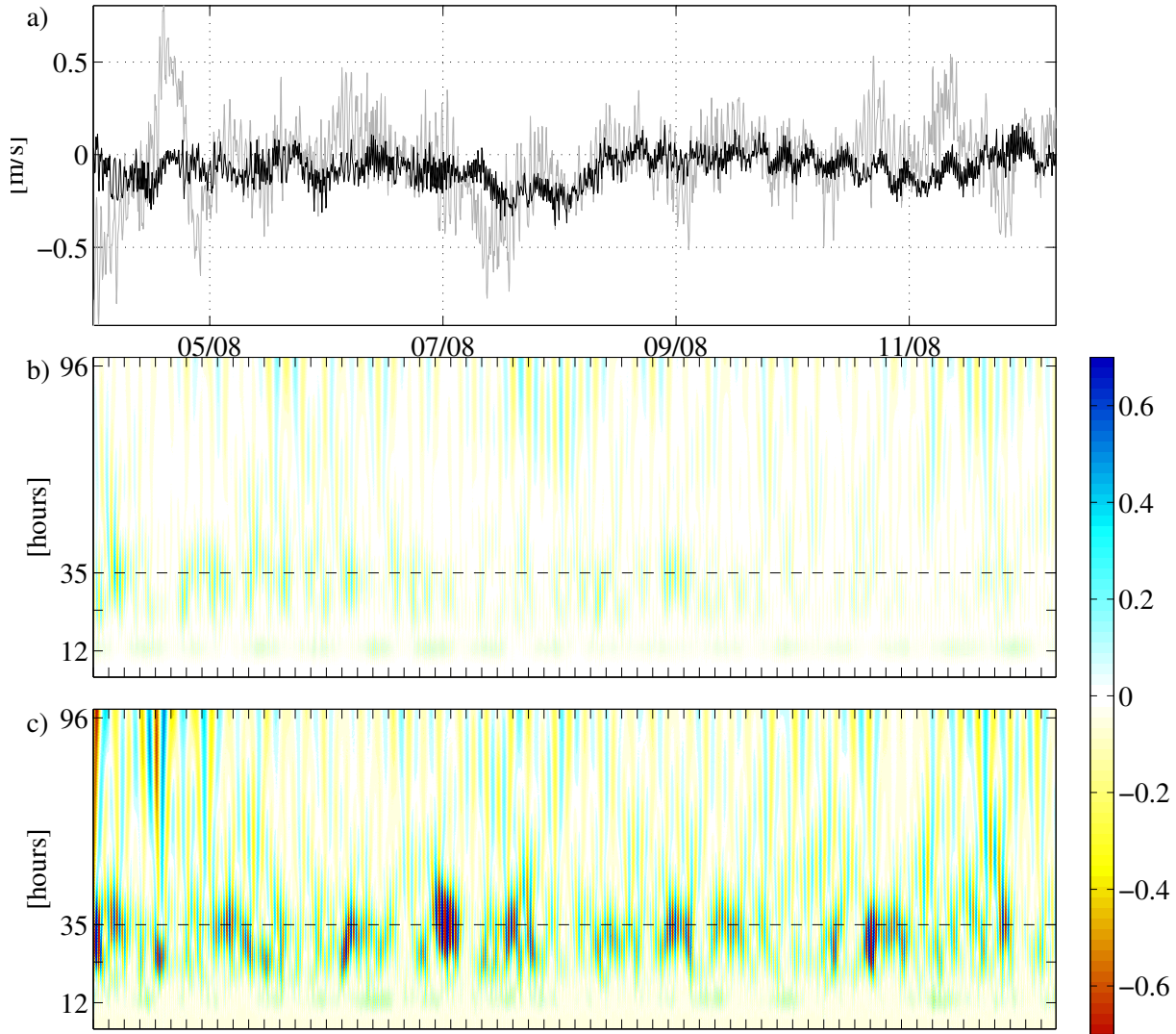


Figure 10. a) Example time series of the surface zonal velocity from FWD (black) and NF08 (grey) experiments at [158.96W, 19.69N]. b) Amplitude scalogram [m/s] for the surface zonal velocity time series from FWD using a 10th order Gaussian wavelet. Ticks along the x-axis indicate the beginning of each assimilation cycle. The inertial frequency for the latitude (35 hours) is marked by the dashed line. c) Same as (b) but from the NF08 time-series.

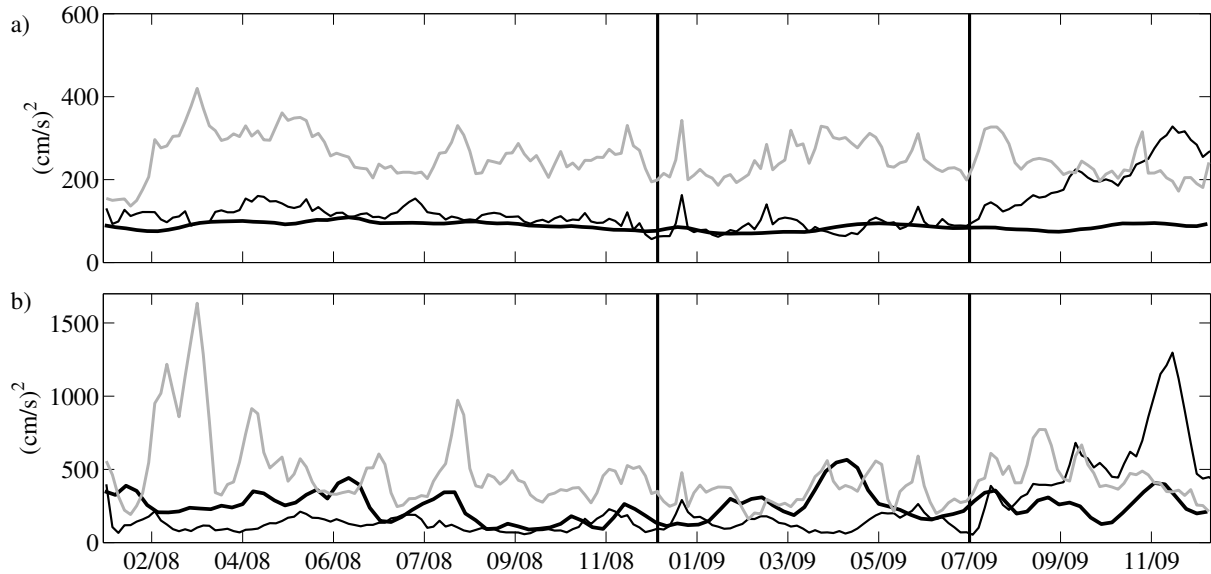


Figure 11. Spatially averaged EKE [$(\text{cm/s})^2$] per experiment cycle from the FWD (thin black line), NF08/F09M/F09W experiments (thin grey line), and the AVISO absolute geostrophic currents product (thick black line). Spatially averaged EKE over the entire domain is shown in a), while in b) only the region in lee of the island of Hawai'i (19°N to 21°N and 156°W to 158.5°W).